Stratocumulus-Driven Cooling in Subtropical Oceans: Contrasting Trends in the Southeast Pacific and South Atlantic

José Vicencio Veloso[1,*], Christoph Böhm[1,*], Felipe Lobos[2,*], Vicente Espinoza Escobedo[2,*], Martin Stengel[3,*], Schöder Mare[3,*], Jan Fokke Meirink[3,*], Jan Schween[1,*], Ulrich Löhnert[1,*], Philipp Breul[1,*], and Susanne Crewell[1,*]

[1]Universität zu Köln
[2]Universidad Católica de Chile
[3]Deutscher Wetterdienst
[*]These authors contributed equally to this work.

Correspondence: José Vicencio Veloso (jvicenc1@uni-koeln.de)

Abstract. Subtropical stratocumulus clouds exert a powerful cooling effect on Earth's climate by reflecting solar radiation, yet their long-term trends and governing mechanisms remain poorly understood. We analyse low cloud fraction, cloud-top height, and liquid water path over 1982–2023 using satellite retrievals, reanalysis, and coastal observations, combining timescale decomposition, ridge regression, and cloud-controlling factor attribution. Our results reveal a stark regional contrast: the Southeast Pacific exhibits multi-decadal stratocumulus expansion (+2.1% decade^{-1} cloud fraction), cloud-top lowering (-167 m decade^{-1}), and surface cooling (-0.2 K decade^{-1}), while the South Atlantic shows negligible changes despite comparable large-scale forcing. Ridge-regularised attribution reveals that boundary-layer stability explains ∼100% of cloud trends in both regions, but surface thermodynamics determine whether this translates into substantial cloud expansion (+33% in the Southeast Pacific) or active opposition (-53% in the South Atlantic). We identify a two-step mechanism in the Southeast Pacific: anticyclone intensification and enhanced lower-tropospheric stability initially cool the surface and strengthen the inversion; the resulting stratocumulus then amplifies cooling through positive shortwave cloud-radiation feedback. The Andes Cordillera enables this feedback by blocking warm continental air intrusions—absent in the South Atlantic, where onshore flow brings continental warming that counteracts stability-driven cloud enhancement. Independent support comes from coastal diurnal temperature trends: daytime maxima cool strongly (-0.4 K decade^{-1}) while nighttime minima remain stable, a fingerprint of shortwave forcing. Climate models underestimate observed Southeast Pacific cooling, likely capturing dynamical forcing but missing cloud-driven amplification, underscoring the need for improved representation of stratocumulus feedbacks in projections.

1 Introduction

Subtropical marine stratocumulus (Scu) clouds dominate subtropical oceans, forming extensive decks that exert a strong shortwave cooling effect on the climate system (Wood, 2012). These clouds contribute substantially to Earth's planetary albedo, and low-cloud feedbacks are a dominant source of uncertainty in estimates of equilibrium climate sensitivity (Zelinka et al.,

2020; Myers et al., 2021). Their persistence is tightly linked to large-scale subsidence, strong lower-tropospheric stability (LTS; Klein and Hartmann 1993), and cool sea-surface temperatures (SSTs) characteristic of the eastern boundary upwelling zones. In the Southeast Pacific, the Andes Cordillera blocks warm continental air intrusions (Xu et al., 2004), creating one of Earth's most extensive stratocumulus decks (Wood, 2012). Given their major role in modulating global climate, tracking how these clouds have changed over recent decades is essential for improving climate projections and understanding regional responses to global warming.

Long-term trends in stratocumulus cover remain uncertain due to discrepancies among datasets and retrieval artifacts (Norris and Evan, 2015). Surface-based observations suggest broad subtropical low cloud decreases from 1954–2008, though observing-system artifacts may partly drive these changes (Eastman et al., 2011). Early satellite records (1980s onward) suggest either no significant long-term change in most subtropical basins or moderate increases concentrated in the Southeast and North Pacific (Norris et al., 2016; Seethala et al., 2015). Seethala et al. (2015) analyzed PATMOS-x (1984–2009) and found positive low cloud trends across most stratocumulus basins, including the Southeast Pacific, Northeast Pacific, and Southeast Atlantic, with decreases mainly in the Northeast Atlantic. Globally, Ceppi et al. (2025) applied a cloud-controlling factor framework to satellite observations (2003–2024) and found an overall low-cloud decrease enhancing planetary solar absorption, driven by cloud feedback, aerosol adjustment, and greenhouse-gas adjustment. The Southeast Pacific stands out as a regional exception: low cloud fraction increased markedly over this period, contributing to a negative shortwave radiative anomaly that locally opposes the global trend (Ceppi et al., 2025).

Concurrent with stratocumulus changes, the Southeast Pacific exhibits marked multi-decadal surface cooling (Falvey and Garreaud, 2009), one of the few regions showing negative near-surface and SST trends under recent global warming. Several studies attribute this cooling substantially to internal climate variability, including the negative phase of the Interdecadal Pacific Oscillation (IPO), which can dominate regional trends over multi-decadal timescales (Falvey and Garreaud, 2009; Watanabe et al., 2024). However, large-ensemble modeling studies demonstrate that the ensemble-mean cooling persists regardless of IPO phase, indicating external forcing as the preeminent driver (Jebri et al., 2020). This external forcing operates through intensified coastal upwelling driven by strengthened alongshore winds (Falvey and Garreaud, 2009; Jebri et al., 2020), themselves linked to poleward expansion of the South Pacific subtropical anticyclone under greenhouse gas and ozone forcing (Gillett and Stott, 2009; Staten et al., 2018; Reboita et al., 2019; Jebri et al., 2020). The South Atlantic, by contrast, shows weaker multi-decadal cooling despite broadly similar large-scale anticyclone forcing (Reboita et al., 2019) and coastal upwelling (Richter and Mechoso, 2004), suggesting additional regional factors govern the contrasting responses.

The observed cooling and cloud enhancement in the Southeast Pacific raise fundamental questions about underlying mechanisms. The strengthening of the lower-tropospheric inversion has been proposed as a key driver of increased low cloud cover (Seethala et al., 2015), with enhanced stability arising from surface cooling and free-tropospheric warming. However, causality may operate in both directions: increased cloudiness can itself induce surface cooling through enhanced shortwave reflection (Clement et al., 2009). In the well-mixed marine boundary layer typical of stratocumulus regions (Wood, 2012), temperature and humidity are strongly coupled throughout the layer. Cloud-induced changes in radiative fluxes can therefore alter surface temperature, potentially reinforcing the inversion and creating a positive shortwave cloud-radiation feedback (Clement et al.,

2009; Espinosa and Zelinka, 2024). This cloud-driven mechanism likely amplifies SST perturbations initiated by wind-driven upwelling and internal variability rather than operating independently (Espinosa and Zelinka, 2024). Current global climate models (GCMs) systematically underestimate the observed Southeast Pacific cooling rates, partly due to insufficient representation of coastal upwelling and weak low cloud-radiation feedbacks (Richter, 2015), underscoring the need for improved observational understanding of these coupled processes. The contrasting behaviour between the Southeast Pacific and South Atlantic – despite similar anticyclone forcing and upwelling systems – suggests that additional regional factors govern cloud-SST coupling, motivating a comparative analysis of these two basins.

We focus on the Southeast Pacific and South Atlantic because they host Earth's most persistent stratocumulus decks under nearly identical forcing – strong subtropical anticyclones, coastal upwelling, and subsidence – yet exhibit contrasting multi-decadal trends in surface temperature and cloud cover. The key topographic difference is the Andes Cordillera along the west coast of South America, which blocks warm continental air intrusions that regularly affect the South Atlantic (Xu et al., 2004). This contrast creates a natural experiment for isolating how topography modulates cloud-SST coupling under comparable large-scale forcing.

We hypothesize that the Southeast Pacific's stratocumulus expansion follows a two-step mechanism: (1) large-scale dynamical forcing – anticyclone intensification and enhanced upwelling – cools the surface and warms up the free-troposphere, strengthening the inversion and resulting in increased cloud cover; (2) the resulting stratocumulus amplifies cooling through positive shortwave cloud-radiation feedback. We further hypothesize that this feedback is suppressed in the South Atlantic by warm continental air intrusions that weaken inversion strength, explaining the divergent responses despite similar large-scale forcing.

To quantify these mechanisms, we combine 42 years of temporally homogeneous observations (1982–2023) with timescale decomposition and ridge-regularised regression within the cloud-controlling factor (CCF) framework (Klein et al., 2017), attributing low cloud fraction trends to individual controlling factors including stability, thermodynamics, winds, and subsidence. Our approach introduces two novel observational constraints: CLARA-A3 – the longest homogeneous satellite cloud record currently available – applied here for the first time to stratocumulus trend attribution, and hourly airport observations along coastal Chile that reveal diurnal cycles of cloud and temperature as an independent fingerprint of shortwave cloud-radiation forcing. Timescale decomposition partitions variance across trend, decadal, and interannual components, enabling assessment of whether cloud-SST coupling and the inferred feedback strength are consistent across timescales or dominated by specific modes of variability.

The paper is organized as follows. Section 2 describes the datasets (satellite retrievals, airport observations, and reanalysis products) and Section 3 describes the methods (cloud-controlling factor framework, ridge regression, and timescale decomposition). Section 4 presents the main results and discussion of the timescale decomposition for cloud properties and stratocumulus drivers, as well as the attribution quantification. Section 5 summarizes the main findings and their implications for understanding subtropical cloud-climate feedbacks.

2 Data

2.1 Gridded data

2.1.1 Cloud products

The primary variable in this study is low-level cloud fraction (CFC_{LOW}), obtained from both the CLARA-A3 satellite dataset (Karlsson et al., 2023b), and the ERA5 reanalysis (Hersbach et al., 2020). CFC_{LOW} represents the fractional coverage of low-level clouds, expressed as a percentage (0–100%; see climatology in Fig. 1a,b), and we use monthly mean values throughout. Although the definition of "low-level" differs slightly between products – CLARA-A3 classifies clouds with top pressure greater than 680 hPa as low-level clouds (Karlsson et al., 2023b), while ERA5 uses clouds where $\sigma = p/p_s > 0.8$ (i.e., pressure exceeding 80% of surface pressure) – this discrepancy has negligible impact on our analysis, as stratocumulus clouds in the Southeast Pacific and South Atlantic have cloud tops almost exclusively below 800 hPa.

To complement CFC_{LOW}, we also analyse cloud-top height (CTH) and liquid water path (LWP). CTH and LWP are directly available from CLARA-A3 as standard cloud products (Karlsson et al., 2023b). For ERA5, LWP is provided as a standard variable. CTH is not available as a direct ERA5 product and is therefore derived from ERA5 model-level data by searching downward from the top of the atmosphere to identify the highest model level where cloud liquid water content exceeds 10^{-3} g kg^{-1}; the corresponding model level is then converted to height using the hypsometric equation and the ERA5 temperature profile.

The CLARA-A3 dataset provides ~~calibrated~~ cloud properties derived from the Advanced Very High Resolution Radiometer (AVHRR) aboard NOAA and EUMETSAT Metop polar-orbiting satellites (Karlsson et al., 2023b). With a horizontal resolution of 0.25° and a temporal coverage spanning 1979–20[illegible] the dataset provides approximately fou[illegible]ily global observations (Karlsson et al., 2023b). We restrict our analysis to 1982–2023 to avoid the incomplete and lower-quality coverage of the AVHRR/[illegible] (1979–1981), and to benefit from the enhanced retrieval accuracy enabled by the five-channel AVHRR/2 instrument — specifically the split-window channel 5 (11.5–12.5 μm) introduced with NOAA-7 — which substantially improves cloud-top temperature and height retrievals (Karlsson et al., 2023b). While passive visible/infrared sensors such as AVHRR can miss low clouds obscured by overlying cloud layers, this limitation is minimal in the subsidence-dominated [illegible]P and South Atlantic, where mid- and high-level clouds are infrequent.

Satellite orbital drift in polar-orbiting platforms causes a gradual shift in the local solar time of observation (Karlsson et al., 2023b). This introduces a diurnal-sampling bias that is especially pronounced for LWP, because this variable exhibits a strong diurnal cycle in subtropical stratocumulus regions, peaking in the early morning and decreasing significantly toward afternoon as solar heating thins the cloud layer. Later [illegible]rpass times therefore systematically sample thinner clouds, producing negative biases or spurious negative trends in retrieved LWP. Additionally, the change in solar zenith angle (SZA) associated with the orbital drift affects visible-channel retrievals of LWP, since higher SZA alters path length and forward scattering, typically leading to underes[illegible]ated optical depth and LWP. CFC_{LOW} and CTH are substantially less sensitive to orbital drift than LWP. CTH is retrieved primarily from thermal infrared channels and is therefore largely insensitive to SZA. CFC_{LOW} is also

relatively stable over the typical stratocumulus diurnal range: while cloud fraction does exhibit a modest diurnal amplitude (generally smaller than that of LWP), the cloud layers themselves remain present, and their presence can be detected with high reliability across both morning and afternoon overpasses.

ERA5 provides a matching horizontal resolution of 0.25° and extends from 1940 to present; for consistency, we use the overlapping period 1982–2023. ERA5 low cloud cover is produced by the IFS cloud scheme ~~and output hourly~~; monthly mean values are computed by averaging over all hourly timesteps. Importantly, ERA5 cloud cover is not directly assimilated but rather diagnosed from the model's cloud parametrisation scheme, which operates on the assimilated atmospheric state. However, since ERA5 assimilates satellite radiances (including cloud-affected channels), the temperature and humidity profiles that drive cloud formation are indirectly constrained by satellite observations. This indirect satellite influence must be considered when comparing ERA5 cloud products with CLARA-A3, though ERA5's physically consistent representation of the full atmospheric column remains a key advantage for process-level attribution.

2.1.2 Atmospheric and oceanic variables

We analyse several atmospheric and thermodynamic variables identified in the literature as key drivers of stratocumulus clouds, all obtained from ERA5 single-level and pressure-level monthly averages for 1982–2023 (Hersbach et al., 2023b, a). These variables are organised into five physically motivated groups to facilitate the cloud-controlling factor attribution framework (Section 3.2):

Surface thermodynamics: Sea surface temperature (SST) and 2 m air temperature (T_{2m}), which characterise surface thermal forcing and boundary-layer base conditions. This group captures surface cooling/warming and its potential role in the cloud-radiation feedback mechanism.

Boundary-layer stability: Boundary layer height (BLH), lower free-troposphere potential temperature (θ_{750}), and lower-tropospheric stability (LTS). LTS is computed as the difference between potential temperature at 750 hPa and 2 m air temperature, where potential temperature is given by $\theta = T(P_0/P)^k$ with k the Poisson constant ($\approx 2/7$), P_0 the surface pressure, and P the pressure at 750 hPa. This group characterises inversion strength and static stability, which govern stratocumulus maintenance and the coupling between surface and cloud-layer processes.

Large-scale dynamics: Sea level pressure (SLP), lower to mid free-troposphere vertical velocity (ω_{500} and ω_{750}), lower free-troposphere horizontal winds (u_{750} and v_{750}), and surface winds (u_{10m} and v_{10m}). This group characterises large-scale subsidence, anticyclone forcing, horizontal advection, and surface wind stress, representing the external dynamical forcing on the boundary layer.

Atmospheric moisture: Total column water vapour (TCWV) and lower free-troposphere specific humidity (q_{750}), which characterise column-integrated and free-tropospheric moisture content. This group captures the influence of atmospheric humidity on cloud formation, entrainment, and radiative processes.

All drivers: The complete set of controlling factors (SST, T_{2m}, LTS, BLH, T_{750}, SLP, ω_{500}, ω_{750}, u_{750}, v_{750}, u_{10m}, v_{10m}, TCWV, q_{750}), used to assess the combined explanatory power of all meteorological drivers and to partition variance across individual versus combined influences.

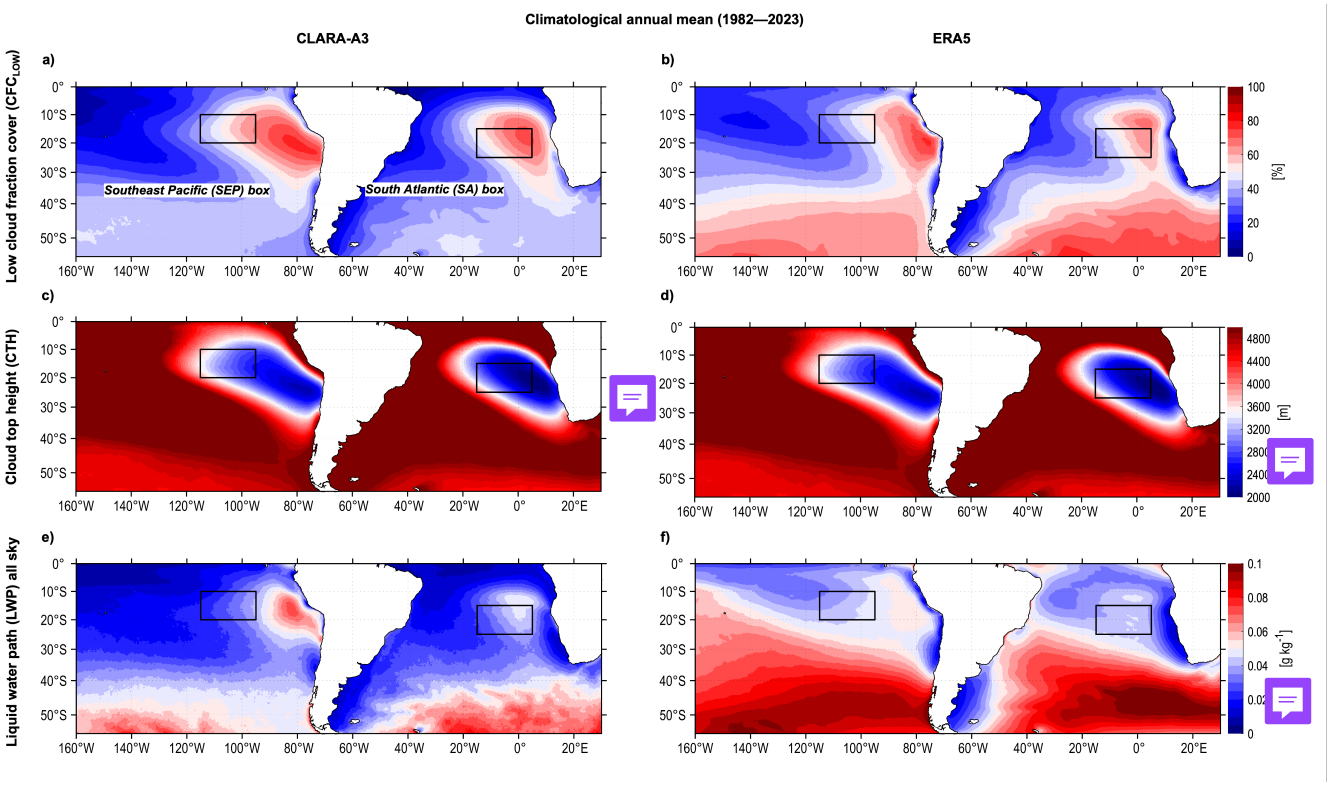

Figure 1. 1982–2023 annual mean climatology of strat[illegible]ulus properties derived from CLARA-A3 (left panels) and ERA5 (right panels) for CFC_{LOW} (a,b), CTH (c,d) and LWP (e,f). The SEP and SA boxes are plotted in black boxes on all panels. Continents are patched white.

2.2 In situ data

We complement the gridded datasets with surface observations of total cloud cover (TCC) and 2 m air temperature from seven coastal airports in Chile between 18 and 38°S (Arica, Iquique, Antofagasta, La Serena, Rodelillo, Santo Domingo, and Concepción; Fi[illegible]) for 1982–2023. These data consist of hourly reports of total sky cover in oktas (converted to percentages: 8 oktas = 100%) provided by trained human observers. The stations are located within 1–10 km of the coastline, with the northern stations (Arica, Iquique, Antofagasta) situated adjacent to the ocean and blocked to the east by the coastal cordillera, making them particularly sensitive to MBL conditions and offshore air temperature changes.

Several limitations must be noted. First, the observations do not distinguish cloud types or altitudes; TCC includes all clouds, whereas low cloud fraction refers specifically to low-level clouds. Second, data are restricted to Southeast Pacific coastal sites, with no equivalent airport records available for the Namib region in the South Atlantic. Third, human observer subjectivity can introduce small inconsistencies, though standardised training and procedures minimise this effect. Despite these constraints, the in situ records provide a valuable independent constraint on gridded products, particularly for validating coastal low cloud

trends and extracting the diurnal cycle of cloud and temperature changes in the Southeast Pacific – a critical test of the proposed shortwave cloud-radiation feedback mechanism.

3 Methodology

This section describes the methods used to quantify long-term trends and variability in stratocumulus clouds and their large-scale drivers in the Southeast Pacific and South Atlantic. All analyses – including timescale decomposition, trend estimation, and ridge-regularised regression – are performed separately on two predefined regional boxes: the Southeast Pacific (SEP) box, centered on the main stratocumulus deck offshore of the Atacama Desert (20–30°S, 75–85°W), and the South Atlantic (SA) box, centered on the main deck offshore of the Namib Desert (10–20°S, 0–10°E; Fig. 1a). These boxes are chosen to capture the core regions of persistent low clouds while minimising influence from coastal transitions and cumulus zones.

3.1 Timescale decomposition and trends

To isolate physically distinct timescales in the regional cloud variables ($\mathrm{CFC_{LOW}}$, CTH, and LWP), we apply a timescale decomposition following Greene et al. (2011). The method separates variability into trend, decadal, and interannual components, ensuring that short-term fluctuations do not artificially influence the long-term trend, and vice versa.

The procedure is as follows. First, annual-mean anomalies are computed for each region by removing the climatological seasonal cycle over 1982–2023, yielding the full time series $Y(t)$. Second, the *trend component* $Y_{\mathrm{trend}}(t)$ is obtained by regressing $Y(t)$ onto a low-pass filtered global mean surface temperature (GMST) series (GISTEMP Team, 2025; Lenssen et al., 2024). Regressing onto GMST rather than year isolates the long-term forced signal and reduces the influence of internal variability on the trend estimate. Third, the detrended series $Y_{\mathrm{detrend}}(t) = Y(t) - Y_{\mathrm{trend}}(t)$ is computed. Fourth, the *decadal component* $Y_{\mathrm{decadal}}(t)$ is extracted by applying a fourth-order low-pass Butterworth filter with a 10-year cutoff period to the detrended series. Finally, the *interannual component* is defined as the residual: $Y_{\mathrm{interannual}}(t) = Y_{\mathrm{detrend}}(t) - Y_{\mathrm{decadal}}(t)$.

The explained variance of each component is quantified via the coefficient of determination R^2. The R^2 values for the three components sum to approximately 1, accounting for the total variability in the original time series.

It is important to note that the trend component derived from the decomposition is used solely to isolate timescales and quantify variance contributions. Linear trends reported elsewhere in this study are estimated independently via ordinary least squares applied to the full time series of cloud variables and stratocumulus drivers.

3.2 Ridge regression

To quantify the contribution of atmospheric drivers to $\mathrm{CFC_{LOW}}$ variability and trends, we employ ridge-regularised linear regression with time-series cross-validation. Ridge regression is preferred over ordinary least squares because meteorological predictors exhibit substantial multicollinearity, which inflates coefficient variance and yields unstable estimates. The 14 ERA5 variables described in Section 2.1.2 are organised into five physically motivated groups for the attribution analysis: *Surface winds*, *Free-tropospheric winds*, *Free-tropospheric subsidence*, *Thermodynamics*, and *Stability parameters*. An *All drivers*

group combines all 14 variables to evaluate total explanatory power. All predictors and the $\mathrm{CFC}_{\mathrm{LOW}}$ response variable are standardised to zero mean and unit variance prior to fitting.

The ridge estimator minimises the penalised residual sum of squares:

$$\hat{\beta} = \arg\min_{\beta} \left\{ \sum_{i=1}^{n} (y_i - \mathbf{x}_i^T \beta)^2 + \lambda \sum_{j=1}^{p} \beta_j^2 \right\} \tag{1}$$

where y_i is the standardised $\mathrm{CFC}_{\mathrm{LOW}}$ for year i, $\mathbf{x}_i$ is the standardised predictor vector, β is the coefficient vector, n is the sample size (42 years), p is the number of predictors, and $\lambda \geq 0$ is the regularisation parameter. Larger values of λ shrink coefficients toward zero, reducing variance at the cost of introducing some bias. This bias-variance trade-off is essential for obtaining stable estimates when predictors are correlated.

The optimal λ is selected via forward-chaining cross-validation, which preserves the temporal ordering of the data and prevents information leakage from future observations into model training. Fifty logarithmically spaced candidate values spanning $\lambda \in [10^{-6}, 10^{4}]$ are evaluated. For each candidate λ, the model is first trained on the initial 60% of the time series (1982–2007), then iteratively retrained by sequentially adding one year at a time and evaluating out-of-sample performance at each step. The value of λ that maximises the mean cross-validated R^2 across all temporal splits is retained for the final model. This procedure is applied independently to each region (SEP and SA boxes) and each predictor group.

Two metrics characterise driver contributions. First, the coefficient of determination R^2 quantifies the fraction of $\mathrm{CFC}_{\mathrm{LOW}}$ variance explained by each predictor group on the full time series. Second, the absolute trend contribution of predictor j to the $\mathrm{CFC}_{\mathrm{LOW}}$ trend is:

$$T_j^{\mathrm{abs}} = \beta_j \cdot \frac{\sigma_Y}{\sigma_{X_j}} \cdot \tau_j \tag{2}$$

where β_j is the standardised ridge coefficient for predictor j, τ_j is the linear trend of predictor j estimated by ordinary least squares (in units per decade), σ_{X_j} is the standard deviation of predictor j (computed from detrended anomalies), and σ_Y is the standard deviation of $\mathrm{CFC}_{\mathrm{LOW}}$ (computed from detrended anomalies). The term σ_Y / σ_{X_j} converts the standardised coefficient to original $\mathrm{CFC}_{\mathrm{LOW}}$ units (% per unit change in X_j), and multiplication by τ_j yields the predicted $\mathrm{CFC}_{\mathrm{LOW}}$ trend attributable to predictor j (% per decade). We also report the relative contribution to the trend, defined as $(T_j^{\mathrm{abs}} / \tau_Y) \times 100\%$, where τ_Y is the observed $\mathrm{CFC}_{\mathrm{LOW}}$ trend. The sum of all relative contributions approximates 100% when the ridge model adequately captures the observed trend, with deviations arising from regularisation bias and nonlinear effects not captured by the linear model.

A critical assumption underlying this approach is stationarity: the sensitivities $\partial \mathrm{CFC}_{\mathrm{LOW}} / \partial X_j$ estimated from interannual co-variation are assumed to govern the multi-decadal response as well. This assumption is standard in cloud-controlling factor frameworks (Klein et al., 2017) and is supported by the substantial trend component identified in Section 4.2. However, if physical relationships between $\mathrm{CFC}_{\mathrm{LOW}}$ and its drivers change on decadal timescales (e.g., due to regime shifts or nonlinear feedbacks), the attribution may underestimate or overestimate certain contributions.

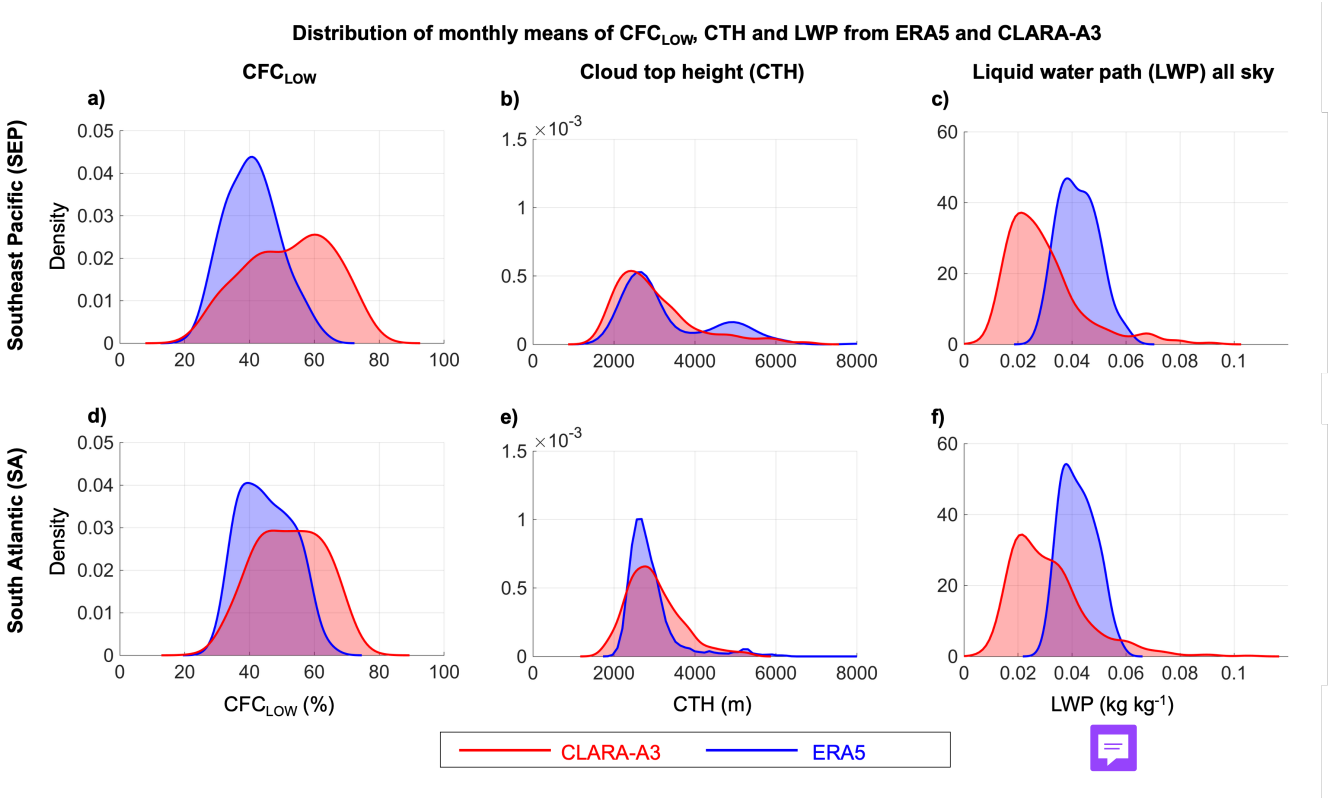

Figure 2. Density distribution of the monthly means of CFC_{LOW}, CTH and LWP for the Southeast Pacific (SEP) box (upper panels) and South Atlantic (SA) box (bottom panels). Values are taken from January 1982 to December 2023 from CLARA-A3 (red) and ERA5 (blue).

4 Results and Discussions

4.1 Mean state

In this section, we first establish a baseline by comparing the climatology of CFC_{LOW}, CTH, and LWP between the CLARA-A3 and ERA5 over 1982–2023 (Fig. 1). This intercomparison is necessary because satellite and reanalysis datasets have complementary strengths and limitations that must be understood before interpreting trends.

The annual-mean CFC_{LOW} climatology shows strong agreement between CLARA-A3 and ERA5 in both basins, with the highest values centered offshore the west coastlines of the continents (Fig. 1a,b). Both datasets correctly capture the core regions of persistent stratocumulus. However, ERA5 exhibits a reduced westward extent compared to CLARA-A3 and a greater poleward extension south of 35°S, where mid and high-level clouds from midlatitude storm tracks become more frequent (Fig. 1d). Conversely, CLARA-A3 underestimates CFC_{LOW} in these southern regions due to occlusion by higher clouds, a well-known limitation of passive visible/infrared satellite retrievals (Karlsson et al., 2023b). The distribution of monthly means

of CFC_{LOW} within the SEP and SA boxes (Fig. 2a,d) shows similar representation of lower cloud fractions in both products, but CLARA-A3 reaches higher peak values, indicating that ERA5 tends to underestimate maximum cloud cover frequency.

The CTH climatology also shows consistent spatial structure between CLARA-A3 and ERA5, with the lowest cloud tops in core regions and increasing values toward the edges (Fig. 1c,d). Both datasets indicate similar CTH medians in the SA and SEP boxes, roughly 2500–3000 m (Fig. 2b,e). ERA5 detects higher clouds, showing a second peak around 5000 m (clearer in the SEP than SA) due to summer continental convection that brings mid-tropospheric clouds to the region.

LWP peaks offshore at 10–20°S, with higher values in the Southeast Pacific than the South Atlantic (Fig. 1e,f). ERA5 median LWP is nearly twice CLARA-A3's in both boxes (Fig. 2c,f), suggesting thicker clouds despite lower cloud fraction, though CLARA-A3 distributions reach higher peak values. These patterns align with previous subtropical Scu climatologies (Wood, 2012), confirming both datasets capture LWP's essential spatial characteristics despite magnitude differences. We note jumps in the CLARA-A3 LWP time series from satellite transitions and orbital drift (Karlsson et al., 2023b) compromise trend reliability; consequently, we use only ERA5 for LWP trends.

The differences between CLARA-A3 and ERA5 arise primarily from their inherent limitations. ERA5's coarse resolution (∼31 km) limits fine-scale dynamics resolution, contributing to CFC_{LOW} underestimation in stratocumulus regions (Zhang et al., 2024; Hersbach et al., 2020). ERA5 may overestimate LWP to compensate for lower cloud fraction. Conversely, CLARA-A3 is more sensitive to low clouds but suffers from high-cloud occlusion and orbital drift biases, particularly in LWP retrievals (Karlsson et al., 2023b). These complementary strengths justify combined use: CLARA-A3 for CFC_{LOW} and CTH, ERA5 for physically consistent LWP time series.

4.2 Interannual, decadal and trend variability

A central question when interpreting long-term changes in subtropical stratocumulus is the extent to which observed variability arises from multi-decadal trends versus shorter-term natural fluctuations. To address this, we decompose the annual-mean anomalies of CFC_{LOW}, CTH, and LWP (relative to the 1982–2023 climatology) into trend, decadal, and interannual components for both the SEP and SA boxes (Fig. 3).

In the SEP box, interannual variability dominates CFC_{LOW} anomalies (48.7% of variance), but the long-term trend is substantial and statistically significant: +2.1% decade^{-1}, accounting for 41.3% of the total variance (Fig. 3a). The decadal component is minor (2.9%). CTH shows a strong negative trend (-167.0 m decade^{-1}, 29.0%), with interannual variability again dominant (48.6%; Fig. 3b). LWP exhibits a significant positive trend (∼1.0 g m^{-2} decade^{-1}, 21.9%), with interannual variability dominant (44.6%) and a larger decadal component (36.9%; Fig. 3c). Notably, CFC_{LOW} and LWP show visibly larger year-to-year fluctuations after 2009.

The SA box presents a contrasting picture. Interannual variability dominates CFC_{LOW} even more strongly than in the SEP (62.4%), with the trend contributing only 5.4% (+0.6% decade^{-1}; Fig. 3d). The decadal component is larger (29.5%), suggesting more pronounced multi-decadal oscillations. CTH shows a significant negative trend (-104.5 m decade^{-1}, 24.6%), though its relative contribution to variance is also lower than in the SEP (Fig. 3e). LWP is dominated by interannual variability (57.1%), with essentially no trend (∼0.01 g m^{-2} decade^{-1}, 3.1%) and a substantial decadal component (30.7%; Fig. 3f).

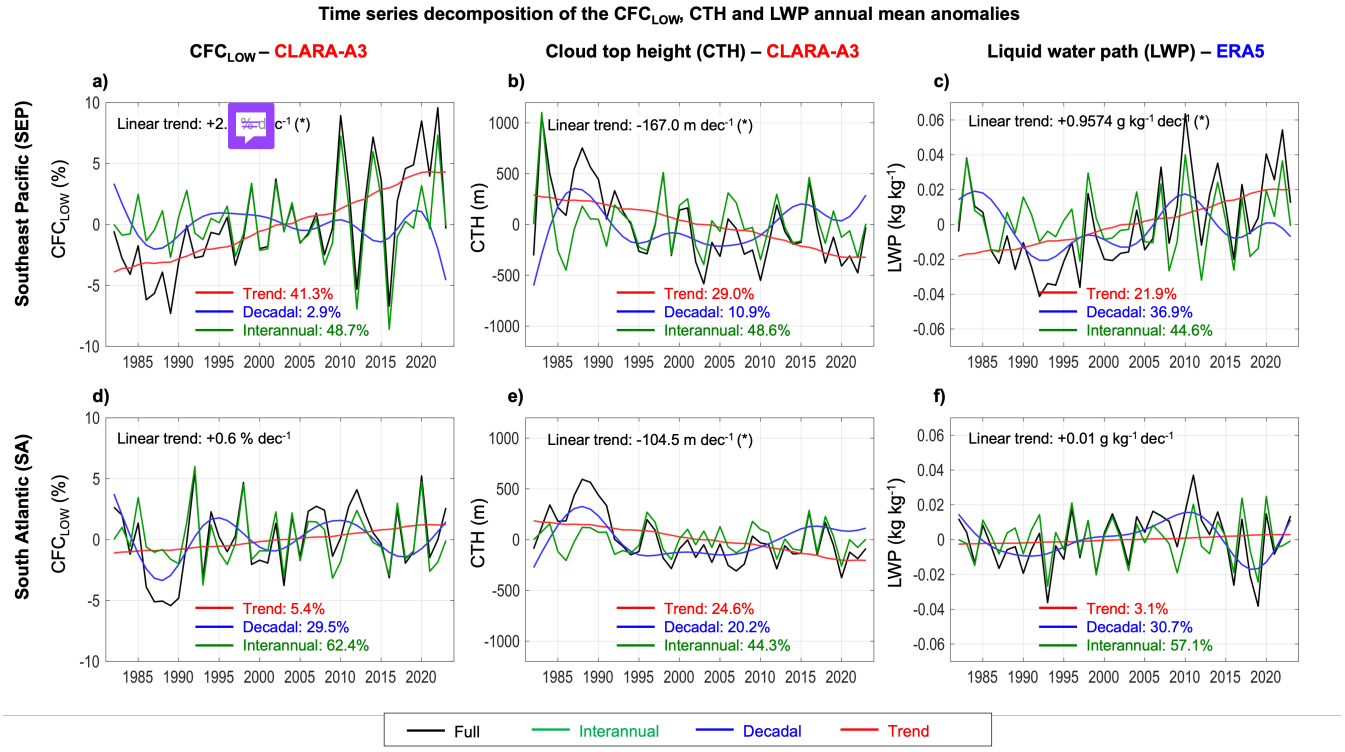

Figure 3. Time series decomposition of CFC_{LOW} (a,d) and CTH (b,e) from CLARA-A3 and LWP (c,f) from ERA5 for the Southeast Pacific box (upper panels) and South Atlantic box (bottom panels).

These decompositions reveal a marked regional contrast: in the SEP box, a substantial fraction of the variance in all three cloud properties is captured by a coherent multi-decadal trend (more frequent, lower-topped, and thicker clouds), whereas in the SA box the same variables are mostly controlled by interannual and decadal fluctuations, with little evidence of a comparable long-term shift. The significant lowering of cloud tops is a shared feature, but its relative importance is greater in the SEP. This finding justifies a closer examination of the spatial patterns and seasonal structure of the trends, particularly in the Southeast Pacific, where the multi-decadal signal is strong (Fig. 4).

CFC_{LOW} exhibits a marked positive trend across most of the Southeast Pacific in both CLARA-A3 and ERA5, with local rates reaching 3% decade^{-1} (Fig. 4a,b). This increase is accompanied by westward and southward expansion of the Scu region (CFC_{LOW} >50%), which has grown at 5.5% decade^{-1} between 1982–1991 and 2014–2023. LWP also increases significantly, with areas where LWP exceeds 5.0 g m^{-2} expanding proportionally (4c,d). Meanwhile, CTH decreases markedly along the western and southern edges of the Scu region, at rates of 100–400 m decade^{-1} (Fig. 4e,f).

These concurrent changes are physically consistent. The cloud frequency rise manifests through increased liquid water content and, predominantly, cloud-top lowering. The pronounced decrease in CTH suggests a shift in the cloud regime toward conditions more favorable for stratocumulus. In the SEP, low clouds typically transition from stratocumulus to cumulus moving

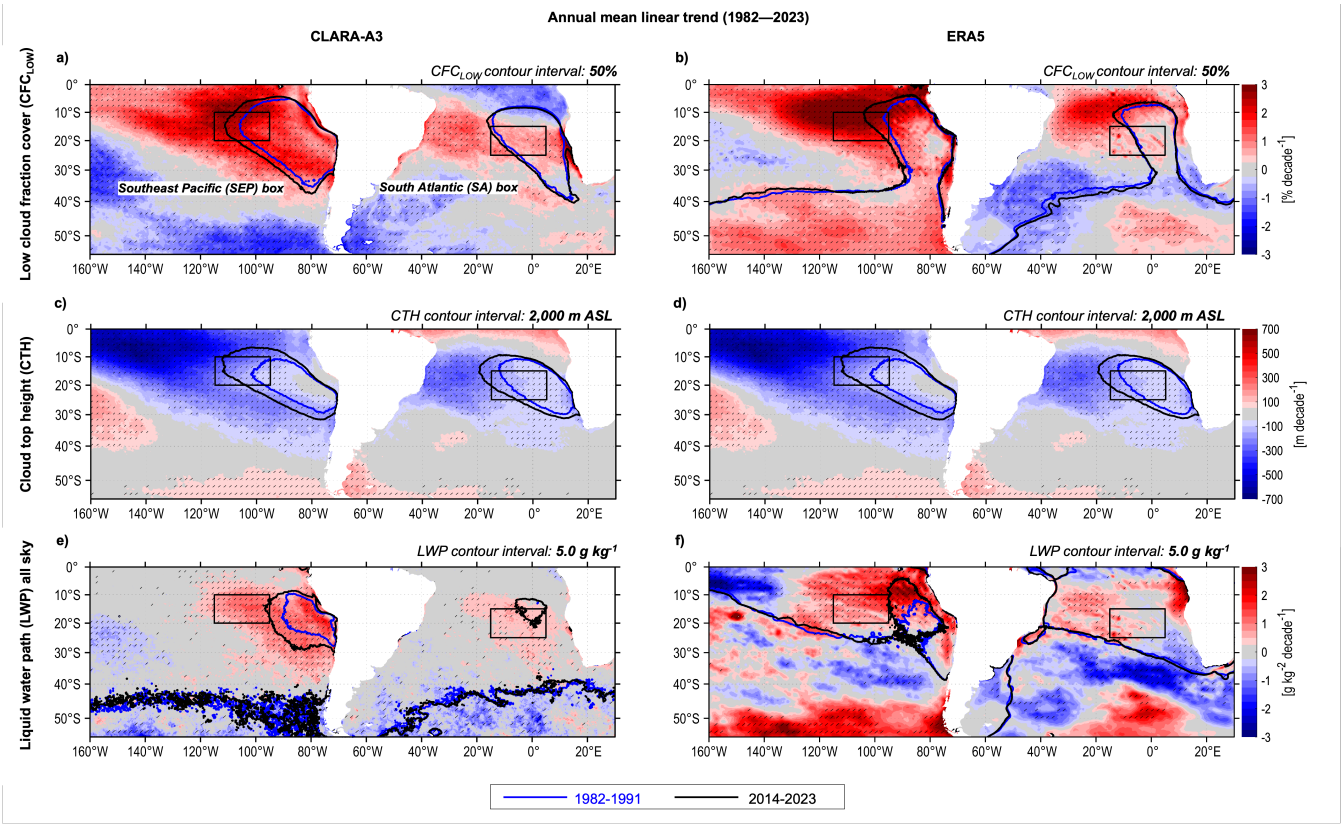

Figure 4. 1982–2023 annual mean linear trend of stratocumulus properties derived from CLARA-A3 (left panels) and ERA5 (right panels) for CFC_{LOW} (a,b), CTH (c,d) and LWP (e,f). Areas with black dots indicate statistical significance at a confidence level of 95%. For panels a, b, c, and d, we include the contour of short-term climatology of the variable for 1982–1991 (blue) and 2014–2023 (black). The SEP and SA boxes are plotted in black boxes on all panels. Continents are patched white.

westward from the coast (Wood, 2012). The observed trends indicate the stratocumulus regime is expanding westward and southward, with the Sc⟶Cu transition zone shifting offshore. This explains the CTH reduction and the expansion of lower CTH values (stronger, more uniform stratocumulus replacing transitional or cumulus clouds).

Seasonal analysis shows Scu expansion and CFC_{LOW} increase occur year-round but peak during austral autumn (MAM) in the Southeast Pacific, when the Scu region expands at 8.2% decade^{-1} and CFC_{LOW} increases at 2.4% decade^{-1}. The CTH decrease is also strongest in autumn, nearly doubling the annual rate to -336 m decade^{-1}. Although LWP shows positive trends, they are not statistically significant in autumn; the strongest LWP trends occur in winter (JJA).

In the South Atlantic, CFC_{LOW} increase is confined mainly to the Namibian coastline (up to 5% decade^{-1}) and west of the Scu region (near Brazil), while the equatorial sector (0–10°S) shows negative trends. Overall, the South Atlantic shows weak positive trends in low cloud frequency, leading to minimal expansion of the Scu region and slight changes in LWP. As

in the Southeast Pacific, the strongest trends occur in the austral autumn. Despite this, CTH shows significant negative trends, suggesting possible cloud regime changes are also occurring in this region.

4.3 Trends in stratocumulus drivers

The timescale decomposition revealed that multi-decadal trends dominate stratocumulus evolution in the Southeast Pacific but play a minor role in the South Atlantic. We now examine the large-scale atmospheric changes accompanying these contrasting cloud trends, focusing on spatial patterns of key drivers over 1982–2023 (Fig. 5).

SLP strengthens in both basins, most pronounced on the poleward flank of the anticyclones and particularly in the Southeast Pacific (up to 0.5 hPa decade^{-1}; Fig. 5a). This intensification, consistent with Hadley cell poleward expansion (Gillett and Stott, 2009; Staten et al., 2018; Reboita et al., 2019), coincides with strengthening trade winds across both basins ($\sim$0.2 m s^{-1} decade^{-1}; Fig. 5b), reflecting the enhanced meridional pressure gradient.

Marine BLH increases in both basins, with a stronger trend in the Southeast Pacific ($\sim$40–60 m decade^{-1}; Fig. 5c). This deepening coincides spatially with intensified easterlies, suggesting that stronger trade winds transport deeper MBL air masses westward, extending the spatial footprint of stratocumulus-favorable conditions (Wood, 2012).

LTS exhibits positive trends over both core stratocumulus regions, but with markedly different magnitudes: $\sim$0.5 K decade^{-1} in the Southeast Pacific versus $\sim$0.2 K decade^{-1} in the South Atlantic (Fig. 5d). This difference arises from contrasting surface temperature trends. In the Southeast Pacific, surface air temperature and SST both show clear cooling (-0.2 to -0.3 K decade^{-1}; Fig. 5e,f), while free-tropospheric temperature at 750 hPa warms across both basins (Fig. 5g). In the South Atlantic, surface and SST trends are weakly positive to neutral, yielding weaker inversion strengthening despite comparable free-tropospheric warming.

TCWV decreases in the Southeast Pacific in a band extending from the tropics to midlatitudes (Fig. 5h), consistent with anticyclonic expansion. In the South Atlantic, TCWV shows little change within the core stratocumulus region and even increases near the West African coast north of 10°S.

In summary, both basins exhibit similar large-scale dynamical changes – anticyclone intensification, enhanced trade winds, BLH deepening, free-tropospheric warming, and increased LTS. However, surface temperature trends diverge sharply: cooling in the Southeast Pacific versus warming or neutral conditions in the South Atlantic. The vertical structure of these changes and their quantitative contributions to cloud trends are examined in the following sections.

4.4 Attribution of trends to cloud-controlling factors

Before quantifying driver contributions, the vertical structure of the observed trends provides essential physical context for interpreting the regression results (Fig. 6). In the Southeast Pacific, the increase in low clouds is accompanied by MBL cooling that is strongest at cloud top (Fig. 6a,c), exhibiting the vertical structure characteristic of cloud-top longwave radiative cooling (Wood, 2012). The well-mixed MBL transmits this cooling downward through cloud-top radiatively driven convection, producing the broad surface cooling seen in Fig. 5e,f. The MBL also becomes drier (Fig. 6e), as surface cooling reduces

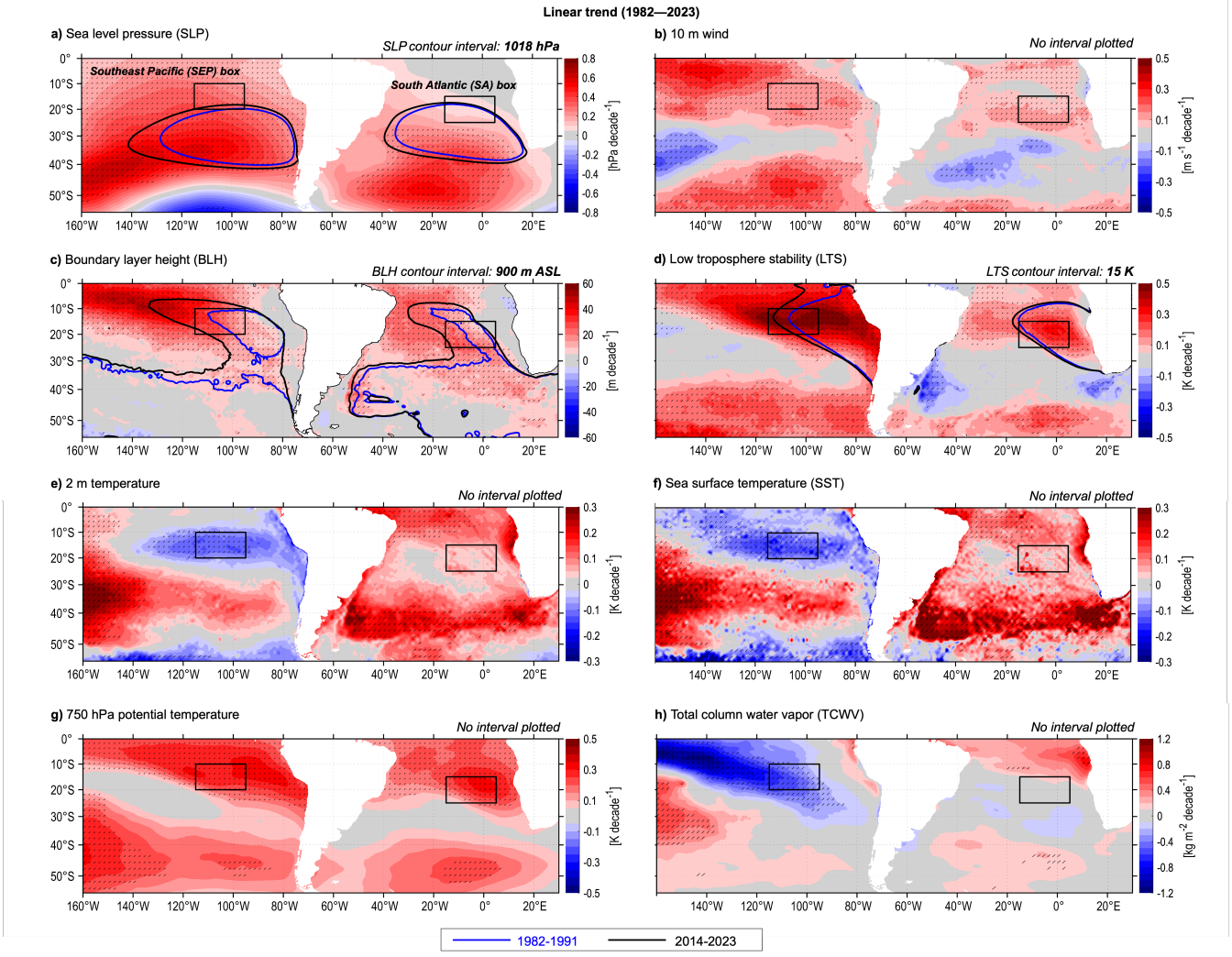

Figure 5. 1982–2023 annual mean linear trend of main stratocumulus drivers of CFC_{LOW} for (a) sea level pressure, (b) 10 m wind, (c) BLH, (d) LTS, (e) 2 m temperature, (f) SST, (g) 750 hPa potential temperature and (h) TCWV. The drivers are derived from ERA5. Areas with black dots indicate statistical significance at the 95% confidence level. For panels (a), (c), and (d) we include the contour of short-term climatology of the variable for 1982–1991 (blue) and 2014–2023 (black). The SEP and SA boxes are plotted in black boxes on all panels. Continents are patched white.

saturation vapour pressure and limits ocean evaporation. Above the stratocumulus layer, free-tropospheric warming and drying coincide with intensified subsidence from the strengthening anticyclone (Fig. 6i), deepening the inversion.

In the South Atlantic, the vertical signals are markedly weaker and less coherent (Fig. 6c,e). Temperature shows only slight cooling near the stratocumulus top, while humidity exhibits drying near the surface but moistening at cloud altitude. Notably, surface winds intensify not only offshore but also over the continent (Fig. 6g), with strengthened onshore flow from the interior.

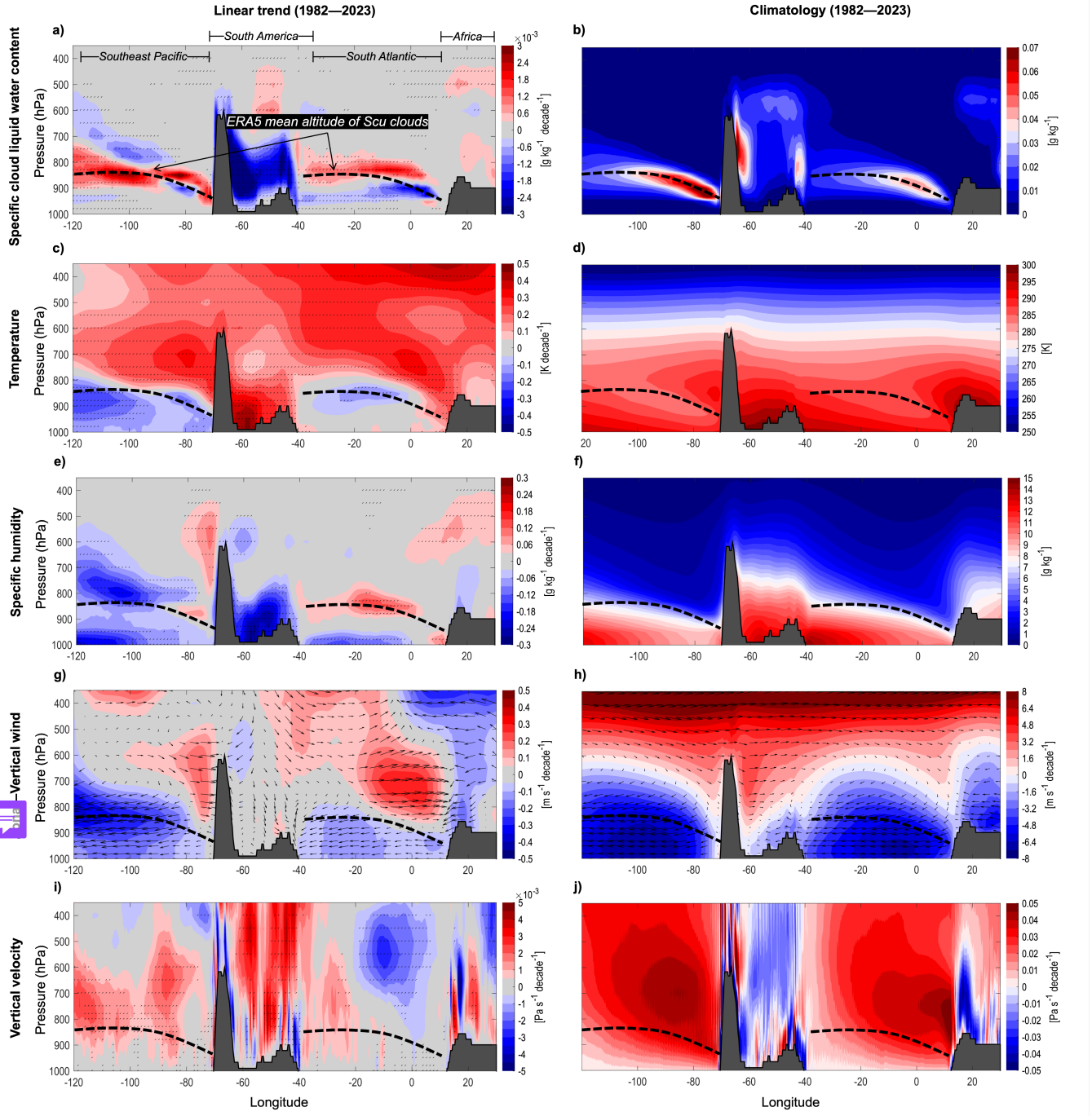

Figure 6. Vertical profiles of the annual mean linear trend (left panels) and annual mean climatology (right panels) for 1982–2023 of ~~specific~~ cloud liquid water content (a,b), temperature (c,d), specific humidity (e,f), zonal-vertical wind (g,h) and vertical velocity (i,j), averaged between 18 and 22°S from 120°W to 30°E. Positive values indicate increases; negative values indicate decreases. Shading shows statistical significance at 95% confidence. The mean altitude of Scu is marked by the dashed line. All variables derived from ERA5.

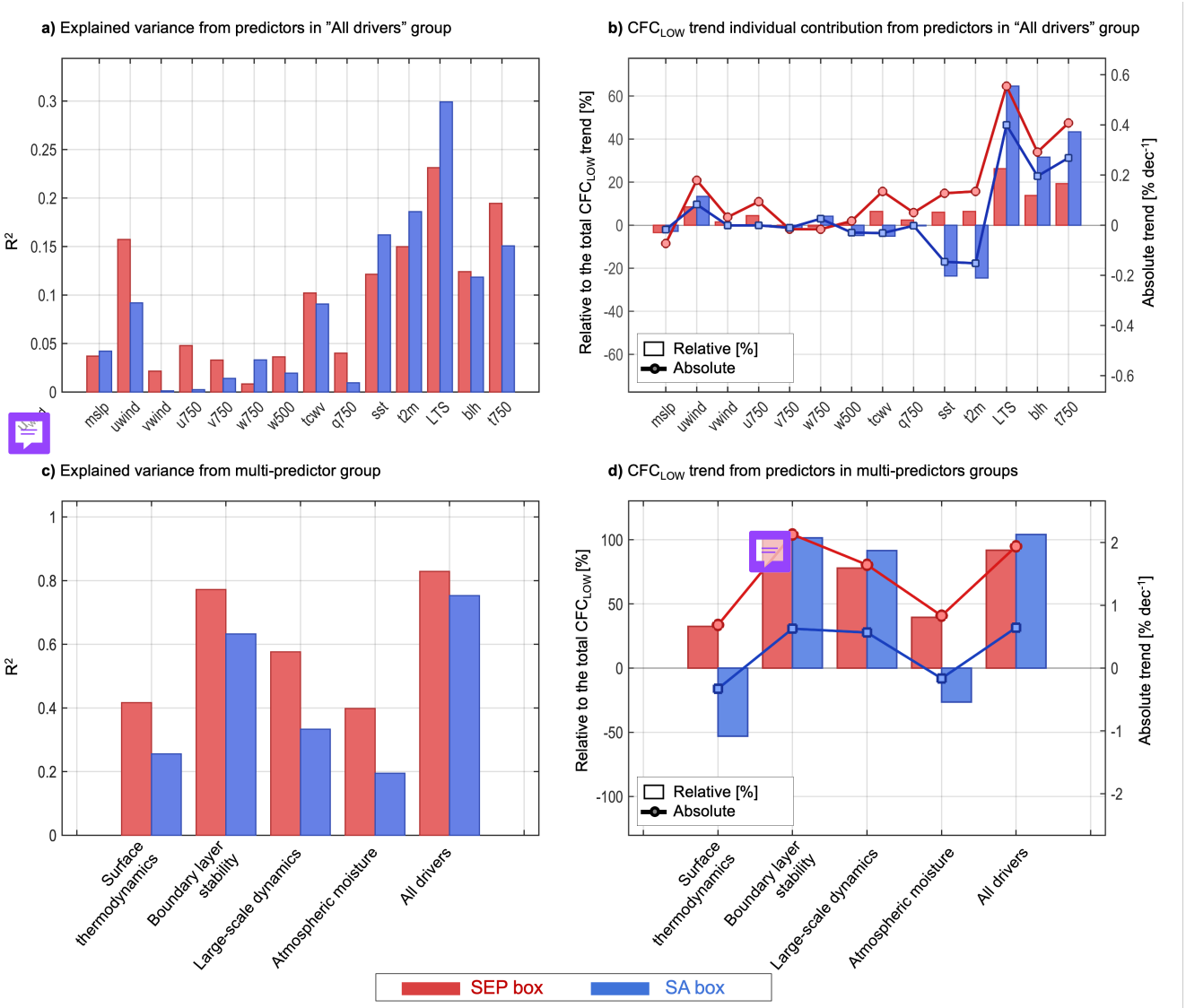

Figure 7. Attribution of CFC_{LOW} trends and variability in the SEP box (red) and SA box (blue) using ridge regression. (a) Explained variance (R^2) of each individual predictor within the "All drivers" group. (b) Absolute trend (line, % dec^{-1}) and relative trend (bar, %) of CFC_{LOW} explained by each individual predictor within the "All drivers" group; the relative trend is expressed as a percentage of the total observed CFC_{LOW} trend in each region. (c) As in (a), but for each independent multi-predictor group. (d) As in (b), but for each independent multi-predictor group. All values are based on the 1982–2023 period.

These differences in vertical structure and wind patterns suggest fundamentally different boundary-layer processes are at work in the two basins, despite similar large-scale anticyclone forcing.

Building on this physical context, we now quantify driver contributions using ridge-regularised linear regression (Fig. 7). Boundary-layer stability emerges as the dominant control on CFC_{LOW} variability in both regions, with the stability group (LTS, BLH, T_{750}) explaining $R^2 = 0.77$ (SEP) and 0.63 (SA) of variance (Fig. 7c) and accounting for approximately 71% of the observed decadal cloud trend in both basins when regressed independently (Fig. 7d). Within the all drivers group, which takes into account all the predictors, LTS is the single strongest individual predictor, contributing 26% (SEP) and 65% (SA) of the trend independently (Fig. 7b). This confirms that thermodynamic stability structure dominates multi-decadal stratocumulus trends, extending the classical LTS–cloud relationship (Klein and Hartmann, 1993) to trend attribution (Seethala et al., 2015; Klein et al., 2017).

However, a stark regional contrast emerges in surface thermodynamics (SST, T_{2m}). When regressed independently, this group contributes $+33\%$ to the SEP cloud trend but -53% to the SA (Fig. 7d), directly reflecting the differing surface-temperature trends documented in Sect. 4.3. In the SEP, surface cooling (-0.19 K decade^{-1}) reduces the boundary-layer saturation deficit and reinforces stability-driven cloud enhancement; in the SA, surface warming ($+0.08$ K decade^{-1}) raises the lifting condensation level and actively opposes the cloud increases that stability forcing alone would drive (Bretherton and Blossey, 2014). This thermodynamic opposition largely explains the SA's more modest net cloud trend (0.62% decade^{-1}) compared to the SEP (2.11% decade^{-1}).

Large-scale dynamics (SLP, subsidence, winds) contribute 78% (SEP) and 92% (SA) of the decadal trend (Fig. 7d), with surface winds (u_{10m}, v_{10m}) providing the largest individual contributions (9% SEP, 13% SA; Fig. 7b). Subsidence shows weaker direct influence (ω_{500} and ω_{750} combined contribute $< 5\%$), suggesting that on multi-decadal timescales large-scale descent exerts influence primarily through modulation of stability structure – already captured by LTS and T_{750} – rather than independent dynamical forcing (Klein et al., 2017). Atmospheric moisture (TCWV, q_{750}) shows a similar sign contrast to surface thermodynamics: $+40\%$ contribution in the SEP versus -26% in the SA (Fig. 7d), reflecting the coupling between temperature and moisture in the well-mixed boundary layer.

The All-drivers model achieves near-complete trend closure in both regions (92% SEP, 104% SA; Fig. 7d), confirming that the selected predictors capture the dominant governing mechanisms. The slight overprediction in the SA suggests additional feedback or nonlinearities that are not fully represented in the linear framework.

The underlying cause of these contrasting responses is ultimately geographical. In the Southeast Pacific, the Andes Cordillera blocks warm continental air intrusions, isolating the MBL and enabling surface cooling, stability enhancement, and stratocumulus expansion to reinforce each other (Xu et al., 2004). In the South Atlantic, the absence of equivalent topographic barriers allows frequent warm continental air exchange (Vicencio Veloso et al., 2024), offsetting anticyclone-driven stability forcing with thermodynamic opposition from surface warming. These topographically controlled differences explain the divergent cloud and temperature responses despite comparable large-scale dynamical forcing, underscoring the critical role of regional geography in cloud–climate feedbacks.

This attribution framework identifies stability forcing as the proximate driver of stratocumulus trends in both basins, but reveals that surface thermodynamics determine whether this stability enhancement translates into substantial cloud increases (SEP) or modest changes (SA). The strong co-occurrence of surface cooling and cloud expansion in the SEP raises a further

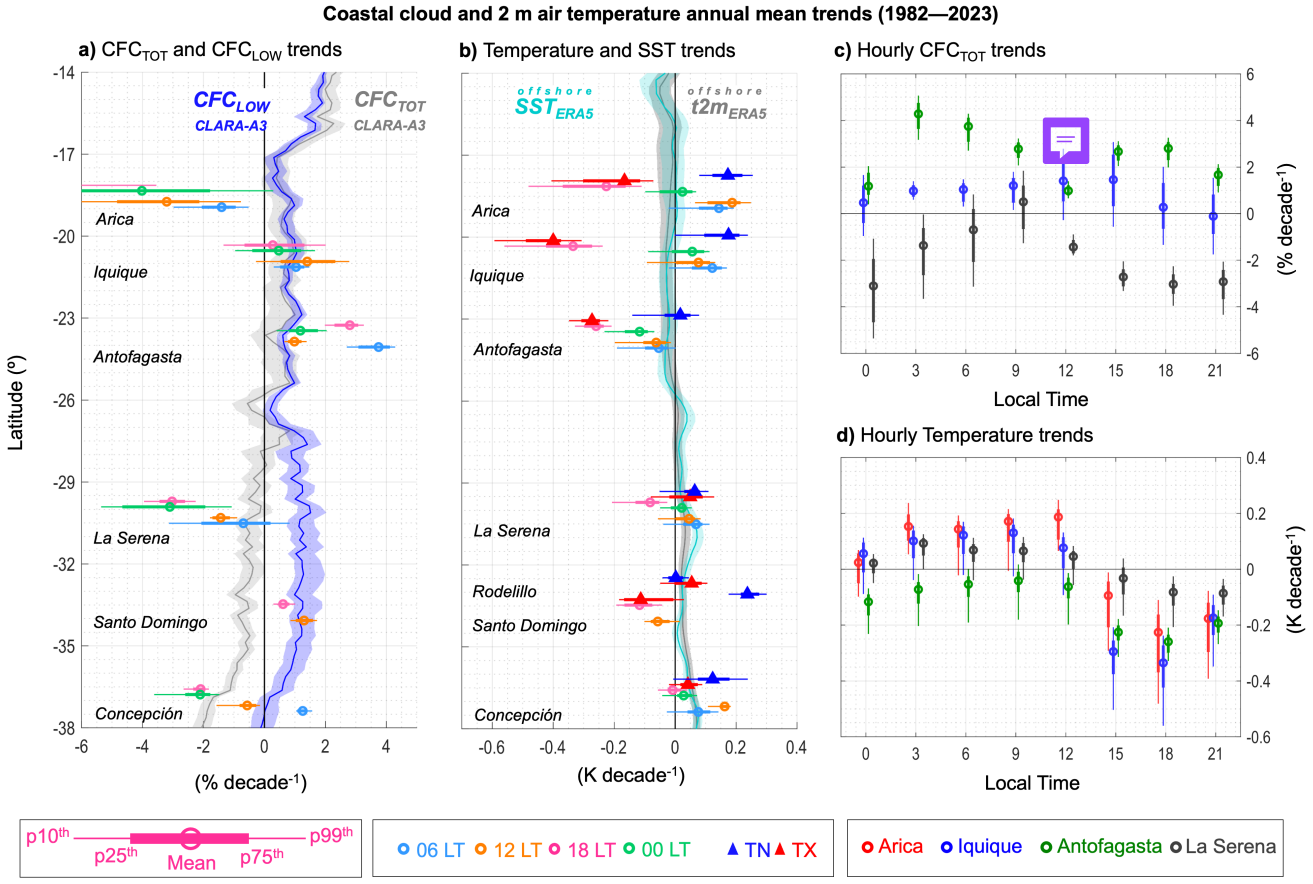

Figure 8. Annual mean trend for 1982–2023 (colored circle) and interquartile range of 30 years moving-window trend (whisker plot) for (a) CFC$_{LOW}$ and CFC$_{TOT}$ derived from CLARA-A3 and airport observations, including the main hours of the day (06, 12, 18, and 00 LT) (b) As in (a), but for the 2m air temperature and SST derived from ERA5. From the airport observations, we included the temperature trends of the main hours of the day, the minimum (TN) and maximum (TX) temperatures. The annual mean of the diurnal cycle of the trends for CFC$_{TOT}$ (c) and 2 m temperature (d), only from airport observations.

question: once established, do the clouds themselves actively reinforce cooling through enhanced shortwave reflection, creating a positive cloud–radiation feedback that amplifies the initial dynamically driven signal? This is the focus of Sect. 4.5.

4.5 The cooling of the Southeast Pacific

The Southeast Pacific exhibits one of the few regions on Earth where near-surface and SST trends have been negative amid global warming, extending from the subtropical stratocumulus region into the equatorial cold tongue. This cooling contrasts sharply with generalized warming elsewhere and with the weak or absent surface cooling in the South Atlantic despite broadly comparable large-scale forcing. As established in Sect. 4.4, the drivers attribution identifies the large-scale dynamical

forcing – anticyclone intensification, enhanced coastal upwelling, and free-tropospheric warming – as the primary trigger for both the inversion strengthening and the subsequent CFC_{LOW} increase. A key remaining question is whether the resulting stratocumulus clouds then actively reinforce the cooling through a positive shortwave cloud-radiation feedback, amplifying the initial dynamically driven signal (Espinosa and Zelinka, 2024; Clement et al., 2009).

To assess this, we examine surface observations from coastal airports along the Chilean coast (18–38°S) over 1982–2023 (Fig. 8). Our observations confirm the continuation of the multi-decadal surface cooling trend previously reported by Falvey and Garreaud (2009) for northern Chile (1979–2006, -0.2 K decade^{-1}) extending it across a broader region with similar magnitude. Cloud fraction trends from airport observations are consistent with those from CLARA-A3: increases of up to 2% decade^{-1} at Iquique and Antofagasta (Fig. 8a), in agreement with previous coastal studies (Muñoz et al., 2016). South of 29°S, station trends show greater variability, reflecting the transition to a zone more frequently influenced by mid-latitude weather systems. At Arica, a strong decrease in cloudiness dominates summer, with slight increases in autumn; moving-window analysis reveals a period of decrease (1982–2000) followed by a reversal to increases (2000–2023), broadly aligning with the CLARA-A3 record and northern stations.

The most diagnostic evidence in this dataset is the diurnal structure of the temperature trend. Daytime maximum temperatures (TX) cool markedly across northern stations (up to -0.4 K decade^{-1} at Iquique), while nighttime minimum temperatures (TN) show slight warming ($+0.2$ K decade^{-1}; Fig. 8b,d). This TX/TN asymmetry – strong daytime cooling alongside weak nighttime warming – is the expected thermodynamic fingerprint of enhanced low-cloud shortwave reflection. Low stratocumulus clouds intercept incoming solar radiation during the day, suppressing surface heating and cooling TX; their effect on outgoing longwave radiation at night is comparatively small, leaving TN largely unaffected or slightly elevated by residual greenhouse effects. In contrast, cooling driven solely by upwelling intensification or large-scale circulation changes carries no inherent diurnal preference in its surface-temperature signal. The strong diurnal modulation of both cloud cover (Fig. 8c) and temperature (Fig. 8d) trends, with cooling peaking at 18 LT following the afternoon maximum in cloud cover, is therefore difficult to explain by dynamical mechanisms alone and is consistent with a shortwave cloud-radiation feedback acting on top of the dynamically driven cooling.

We emphasise that this constitutes observational evidence consistent with a cloud-radiation feedback, not a proof of causality. The co-occurrence of surface cooling, cloud increases, and a diurnally structured temperature response is precisely what such a feedback would produce, but we cannot exclude that a common upstream forcing – such as multidecadal variability in the anticyclone or upwelling – drives both signals independently. Analogous cloud-driven cooling has been identified in the North Pacific using observations and energy budget analysis (Clement et al., 2009), and more recently Espinosa and Zelinka (2024) showed explicitly that the shortwave cloud–SST feedback amplifies multi-decadal Pacific SST trends in the Southeast Pacific, providing a theoretical framework consistent with our findings.

Together, our observational results support a two-step mechanism: large-scale dynamical cooling strengthens the inversion and triggers stratocumulus expansion, after which the resulting clouds amplify the cooling through enhanced shortwave reflection, creating a positive cloud-radiation feedback that reinforces the initial signal. This mechanism offers a physically coherent explanation for why current GCMs systematically underestimate the observed Southeast Pacific cooling. These

models exhibit well-documented biases in simulating subtropical low clouds (Lee et al., 2022; Mechoso et al., 1995), typically underrepresenting cloud fraction and radiative feedbacks in stratocumulus regions. If the cloud-radiation feedback described here is not adequately captured in model physics, the amplification step will be missing, and GCMs will reproduce only the dynamically forced component of the cooling while missing the cloud-driven amplification – consistent with the persistent underestimation reported in the literature (Richter, 2015). Improving the representation of low-cloud feedbacks in GCMs, therefore, remains critical not only for projecting future stratocumulus changes but for correctly simulating observed regional temperature trends in the Southeast Pacific.

5 Summary and conclusions

This study set out to answer a deceptively simple question: why do the Southeast Pacific and South Atlantic – two ocean basins sharing nearly identical large-scale forcing conditions – exhibit such different multi-decadal stratocumulus and surface temperature trends? Using four decades of satellite retrievals, state-of-the-art reanalysis, and independent coastal surface observations (1982–2023), we combined timescale decomposition, spatial trend analysis, vertical profile diagnostics, and ridge-regularised regression to attribute observed changes in stratocumulus clouds' properties to their governing mechanisms. The schematic in Fig. 9 summarises the contrasting pictures that emerge.

The Southeast Pacific exhibits a robust, statistically significant multi-decadal trend toward more frequent, lower-topped, and optically thicker stratocumulus: $\mathrm{CFC_{LOW}}$ has increased at $+2.1\%$ decade^{-1} (accounting for 41.3% of total variance), CTH has decreased at -167 m decade^{-1}, and LWP has increased consistently, accompanied by surface and SST cooling of -0.2 K decade^{-1}. These changes are spatially coherent, seasonally robust (strongest in austral autumn), and consistent across CLARA-A3 and ERA5, lending confidence that they represent a genuine long-term climate signal rather than a retrieval artefact. In the South Atlantic, by contrast, interannual and decadal variability dominate all three cloud variables, with only a weak positive $\mathrm{CFC_{LOW}}$ trend ($+0.6\%$ decade^{-1}, 5.4% of variance) and negligible LWP change – despite the same large-scale dynamical forcing.

The central finding of this paper is the identification of a two-step mechanism linking large-scale dynamics, thermodynamic stability, and cloud-radiation feedbacks in the Southeast Pacific (Fig. 9a). In the first step, large-scale dynamical forcing – anticyclone intensification, Hadley cell expansion, and enhanced coastal upwelling (Gillett and Stott, 2009; Staten et al., 2018; Falvey and Garreaud, 2009; Jebri et al., 2020) – drives surface and SST cooling, which in combination with free-tropospheric warming substantially strengthens the lower-tropospheric inversion (LTS increase of $\sim$0.5 K decade^{-1}). This stability enhancement is the dominant driver of $\mathrm{CFC_{LOW}}$ trends: our ridge regression confirms that the stability parameter group (LTS, t750, BLH, SLP) alone explains 95–105% of the observed decadal cloud trend in both regions, extending the classical LTS–stratocumulus relationship (Klein and Hartmann, 1993) to multi-decadal attribution (Seethala et al., 2015; Klein et al., 2017).

In the second step, the resulting stratocumulus expansion amplifies the initial cooling through a positive shortwave cloud-radiation feedback: increased low-cloud cover intercepts incoming solar radiation, suppressing daytime surface heating and

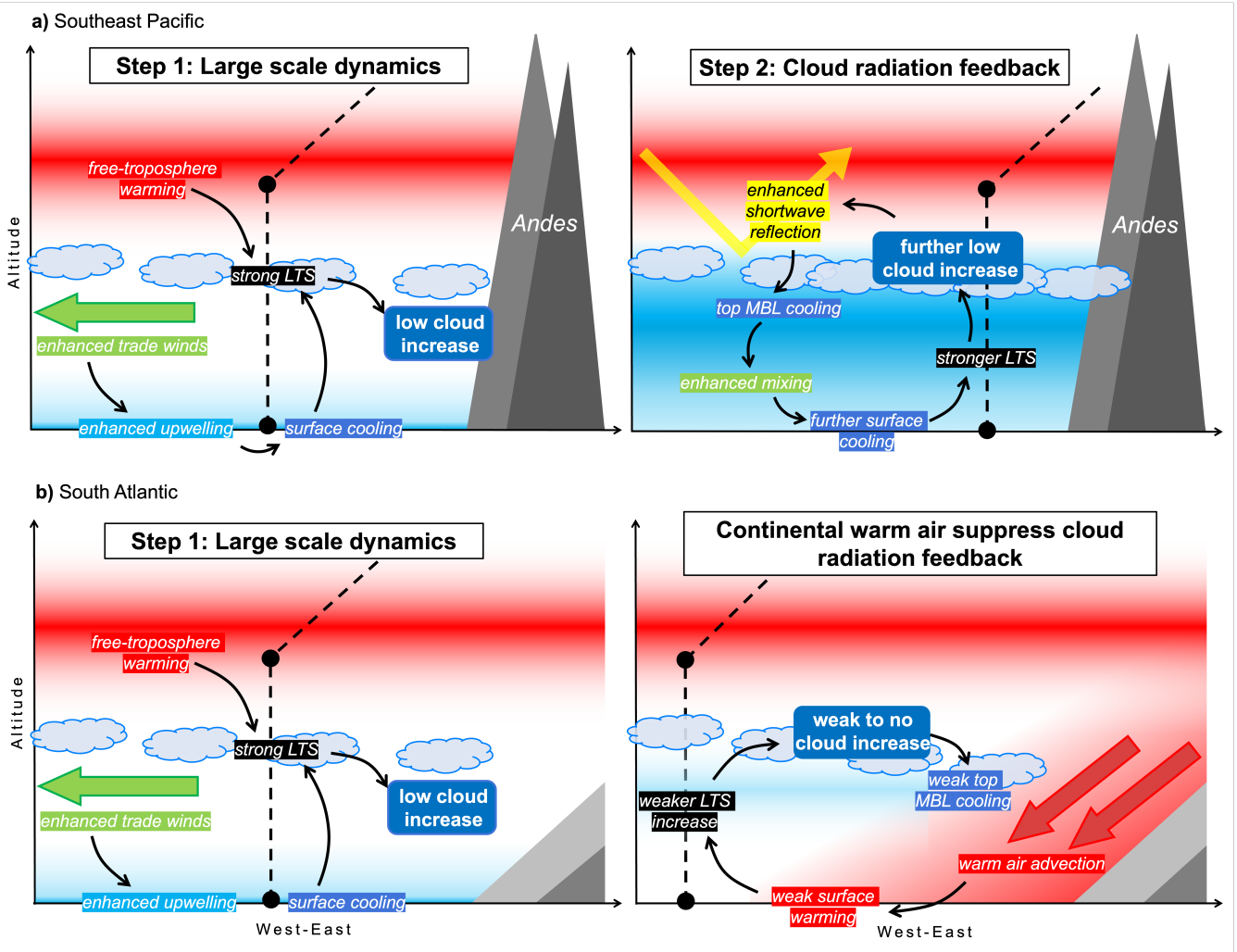

Figure 9. Schen summary of the contrasting long-term stratocumulus trends and drivers in the Southeast Pacific and South Atlantic over 1982–2023. (a) In the Southeast Pacific, a two-step mechanism operates: (1) Large-scale dynamical forcing (anticyclone intensification, free-tropospheric warming/drying, enhanced trade winds) drives surface cooling and LTS enhancement, triggering stratocumulus expansion; (2) The resulting cloud increase amplifies cooling through a positive shortwave cloud-radiation feedback (yellow arrow). The Andes Cordillera blocks warm continental air intrusions, allowing this feedback to operate without disruption. (b) In the South Atlantic, the same large-scale anticyclone forcing is present, but the absence of a topographic barrier allows warm continental air advection, which counteracts stability-driven cloud enhancement, resulting in minimal cloud response and weak surface cooling. Blue elements indicate cooling/cloud-enhancing processes, red elements indicate warming.

further lowering SST, which in turn reinforces the inversion and promotes further cloud formation (Espinosa and Zelinka, 2024; Clement et al., 2009). Crucially, coastal airport observations provide an independent fingerprint of this second step.

The diurnal structure of the temperature trend – strong daytime maximum cooling (~ -0.4 K decade^{-1}) alongside weak nighttime minimum warming – is the expected thermodynamic signature of enhanced shortwave reflection by low clouds, and is difficult to explain by upwelling or large-scale circulation changes alone, which carry no inherent diurnal preference in their surface temperature signal. We emphasise that this constitutes observational evidence consistent with a cloud-radiation feedback rather than a formal proof of causality; however, the diurnal fingerprint, combined with the spatial coherence of the cloud and temperature trends, provides ~~the strongest~~ available observational support for an active cloud contribution to the Southeast Pacific cooling.

The South Atlantic is not merely a region where nothing happens – it is the natural control experiment that isolates the decisive role of regional geography in setting the response to large-scale forcing. The same anticyclone intensification and LTS increase that drive substantial cloud expansion in the Southeast Pacific are present in the South Atlantic, yet produce only a weak cloud trend. The reason is thermodynamic competition: positive SST and surface temperature trends in the South Atlantic raise the lifting condensation level and increase the boundary-layer saturation deficit, actively opposing the stability-driven cloud increase with a net thermodynamic contribution of -46% to the cloud trend – in stark contrast to the reinforcing $+33\%$ thermodynamic contribution in the Southeast Pacific. The underlying cause of this thermodynamic divergence is topographic. The Andes Cordillera isolates the Southeast Pacific MBL from warm continental air intrusions, allowing the cloud-radiation feedback to operate without disruption. In the South Atlantic, the absence of an equivalent barrier allows frequent warm air exchange across the Atlantic MBL (Vicencio Veloso et al., 2024), counteracting the stability-driven cloud enhancement and suppressing the positive feedback loop that characterises the Southeast Pacific. This topographically driven divergence demonstrates that identical large-scale forcing can produce fundamentally different cloud and temperature responses depending on regional geography – a finding with direct implications for how we interpret and model subtropical cloud-climate feedbacks globally.

These findings connect to three open problems in climate science. First, the Southeast Pacific cooling – consistently observed across independent reanalysis, satellite, and surface datasets yet absent in current GCMs (Lee et al., 2022; Mechoso et al., 1995) – is a model evaluation benchmark that specifically tests the representation of shortwave cloud-radiation feedbacks. Our results suggest that GCMs reproduce the dynamically forced component of the cooling but miss the cloud-driven amplification step, because they systematically underestimate low-cloud fraction and the associated radiative response in stratocumulus regions (Richter, 2015). Closing this bias requires not just improved cloud parameterisation but an adequate representation of the MBL isolation mechanism provided by coastal topography.

Second, subtropical stratocumulus feedbacks remain a dominant source of uncertainty in estimates of equilibrium climate sensitivity (Zelinka et al., 2020; Myers et al., 2021). Our observational evidence that the cloud-radiation feedback is active and measurable in the present-day climate of the Southeast Pacific constrains the sign and plausible magnitude of this feedback, complementing process-level studies. Understanding why this feedback is amplified in the Southeast Pacific but suppressed in the South Atlantic provides a natural framework for testing the physical mechanisms that ~~CCF~~-based feedback estimates rely upon.

Third, the recent period of anomalously low planetary albedo and accelerated global surface warming has renewed interest in the role of subtropical low clouds in modulating global energy balance (Goessling et al., 2024). The Southeast Pacific, as one of the largest and most persistent stratocumulus regions on Earth, is a key contributor to global reflected shortwave radiation. Multi-decadal trends in this region, therefore, have implications that extend well beyond regional climate.

Future work should examine how the two-step mechanism identified here evolves under projected warming scenarios, particularly whether the dynamical cooling that currently sustains the positive feedback can persist as greenhouse forcing intensifies, and how aerosol trends and changing continental air mass properties may modulate the topographic isolation effect in both basins.

References

Bretherton, C. S. and Blossey, P. N.: Low cloud reduction in a greenhouse-warmed climate: Results from Lagrangian LES of a subtropical marine cloudiness transition, Journal of Advances in Modeling Earth Systems, 6, 91–114, https://doi.org/https://doi.org/10.1002/2013MS000250, 2014.

Ceppi, P., Wilson Kemsley, S., Andersen, H., Andrews, T., Kramer, R. J., Nowack, P., Wall, C. J., and Zelinka, M. D.: Emerging low-cloud feedback and adjustment in global satellite observations, EGUsphere, 2025, 1–24, https://doi.org/10.5194/egusphere-2025-5206, 2025.

Clement, A. C., Burgman, R., and Norris, J. R.: Observational and model evidence for positive low-level cloud feedback, Science, 325, 460–464, https://doi.org/10.1126/science.1171255, 2009.

Eastman, R., Warren, S. G., and Hahn, C. J.: Variations in cloud cover and cloud types over the ocean from surface observations, 1954–2008, Journal of Climate, 24, 5914–5934, 2011.

Espinosa, Z. I. and Zelinka, M. D.: The Shortwave Cloud–SST Feedback Amplifies Multi-Decadal Pacific Sea Surface Temperature Trends: Implications for Observed Cooling, Geophysical Research Letters, 51, e2024GL111 039, https://doi.org/10.1029/2024GL111039, 2024.

Falvey, M. and Garreaud, R. D.: Regional cooling in a warming world: Recent temperature trends in the southeast Pacific and along the west coast of subtropical South America (1979–2006), Journal of Geophysical Research: Atmospheres, 114, https://doi.org/https://doi.org/10.1029/2008JD010519, 2009.

Gillett, N. and Stott, P.: Attribution of anthropogenic influence on seasonal sea level pressure, Geophysical Research Letters, 36, https://doi.org/https://doi.org/10.1029/2009GL041269, 2009.

GISTEMP Team: GISS Surface Temperature Analysis (GISTEMP), version 4, https://data.giss.nasa.gov/gistemp/, dataset accessed 2025-XX-XX, 2025.

Goessling, H. F., Rackow, T., and Jung, T.: Recent global temperature surge intensified by record-low planetary albedo, Science, 0, eadq7280, https://doi.org/10.1126/science.adq7280, 2024.

Greene, A. M., Goddard, L., and Cousin, R.: Web tool deconstructs variability in twentieth-century climate, Eos, Transactions American Geophysical Union, 92, 397–398, https://doi.org/https://doi.org/10.1029/2011EO450001, 2011.

Hersbach, H., Bell, B., Berrisford, P., Hirahara, S., Horányi, A., Muñoz-Sabater, J., Nicolas, J., Peubey, C., Radu, R., Schepers, D., Simmons, A., Soci, C., Abdalla, S., Abellan, X., Balsamo, G., Bechtold, P., Biavati, G., Bidlot, J., Bonavita, M., De Chiara, G., Dahlgren, P., Dee, D., Diamantakis, M., Dragani, R., Flemming, J., Forbes, R., Fuentes, M., Geer, A., Haimberger, L., Healy, S., Hogan, R. J., Hólm, E., Janisková, M., Keeley, S., Laloyaux, P., Lopez, P., Lupu, C., Radnoti, G., de Rosnay, P., Rozum, I., Vamborg, F., Villaume, S., and Thépaut, J.-N.: The ERA5 global reanalysis, Quarterly Journal of the Royal Meteorological Society, 146, 1999–2049, https://doi.org/https://doi.org/10.1002/qj.3803, 2020.

Hersbach, H., Bell, B., Berrisford, P., Biavati, G., Horányi, A., Muñoz-Sabater, J., Nicolas, J., Peubey, C., Radu, R., Rozum, I., Schepers, D., Simmons, A., Soci, C., Dee, D., and Thépaut, J.-N.: ERA5 hourly data on pressure levels from 1940 to present. Copernicus Climate Change Service (C3S) Climate Data Store (CDS), https://doi.org/10.4225/13/511C71F8612C3, 2023a.

Hersbach, H., Bell, B., Berrisford, P., Biavati, G., Horányi, A., Muñoz-Sabater, J., Nicolas, J., Peubey, C., Radu, R., Rozum, I., Schepers, D., Simmons, A., Soci, C., Dee, D., and Thépaut, J.-N.: ERA5 hourly data on surface levels from 1940 to present. Copernicus Climate Change Service (C3S) Climate Data Store (CDS), https://doi.org/10.4225/13/511C71F8612C3, 2023b.

Jebri, B., Khodri, M., Echevin, V., Gastineau, G., Thiria, S., Vialard, J., and Lebas, N.: Contributions of internal variability and external forcing to the recent trends in the Southeastern Pacific and Peru–Chile upwelling system, Journal of Climate, 33, 10 555–10 578, https://doi.org/https://doi.org/10.1175/JCLI-D-19-0304.1, 2020.

Karlsson, K.-G., Riihelä, A., Trentmann, J., Stengel, M., et al.: CLARA-A3: CM SAF cLoud, Albedo and surface RAdiation dataset from AVHRR data — Edition 3, Satellite Application Facility on Climate Monitoring, https://doi.org/10.5676/EUM_SAF_CM/CLARA_AVHRR/V003, 2023a.

Karlsson, K.-G., Stengel, M., Meirink, J. F., Riihelä, A., Trentmann, J., Akkermans, T., Stein, D., Devasthale, A., Eliasson, S., Johansson, E., Håkansson, N., Solodovnik, I., Benas, N., Clerbaux, N., Selbach, N., Schröder, M., and Hollmann, R.: CLARA-A3: The third edition of the AVHRR-based CM SAF climate data record on clouds, radiation and surface albedo covering the period 1979 to 2023, Earth System Science Data, 15, 4901–4926, https://doi.org/10.5194/essd-15-4901-2023, 2023b.

Klein, S. A. and Hartmann, D. L.: The seasonal cycle of low stratiform clouds, Journal of climate, 6, 1587–1606, https://doi.org/https://doi.org/10.1175/1520-0442(1993)006<1587:TSCOLS>2.0.CO;2, 1993.

Klein, S. A., Hall, A., Norris, J. R., and Pincus, R.: Low-Cloud Feedbacks from Cloud-Controlling Factors: A Review, Surveys in Geophysics, 38, 1307–1329, https://doi.org/10.1007/s10712-017-9433-3, 2017.

Lee, H.-H., Bogenschutz, P., and Yamaguchi, T.: Resolving Away Stratocumulus Biases in Modern Global Climate Models, Geophysical Research Letters, 49, e2022GL099 422, https://doi.org/https://doi.org/10.1029/2022GL099422, e2022GL099422 2022GL099422, 2022.

Lenssen, N., Schmidt, G. A., Hendrickson, M., Jacobs, P., Menne, M., and Ruedy, R.: A GISTEMPv4 observational uncertainty ensemble, Journal of Geophysical Research: Atmospheres, 129, e2023JD040 179, https://doi.org/10.1029/2023JD040179, 2024.

Mechoso, C., Robertson, A., Barth, N., Davey, M., Delecluse, P., Gent, P., Ineson, S., Kirtman, B., Latif, M., Treut, H. L., Nagai, T., Neelin, J., Philander, S., Polcher, J., Schopf, P., Stockdale, T., Suarez, M., Terray, L., Thual, O., and Tribbia, J.: The Seasonal Cycle over the Tropical Pacific in Coupled Ocean–Atmosphere General Circulation Models, Monthly Weather Review, 123, 2825 – 2838, https://doi.org/10.1175/1520-0493(1995)123<2825:TSCOTT>2.0.CO;2, 1995.

Muñoz, R. C., Quintana, J., Falvey, M. J., Rutllant, J. A., and Garreaud, R.: Coastal Clouds at the Eastern Margin of the Southeast Pacific: Climatology and Trends, Journal of Climate, 29, 4525 – 4542, https://doi.org/10.1175/JCLI-D-15-0757.1, 2016.

Myers, T. A., Scott, R. C., Zelinka, M. D., Klein, S. A., Norris, J. R., and Caldwell, P. M.: Observational Constraints on Low Cloud Feedback Reduce Uncertainty of Climate Sensitivity, Nature Climate Change, 11, 501–507, https://doi.org/10.1038/s41558-021-01039-0, 2021.

Norris, J. R. and Evan, A. T.: Empirical removal of artifacts from the ISCCP and PATMOS-x satellite cloud records, Journal of Atmospheric and Oceanic Technology, 32, 691–702, https://doi.org/https://doi.org/10.1175/JTECH-D-14-00058.1, 2015.

Norris, J. R., Allen, R. J., Evan, A. T., Zelinka, M. D., O'Dell, C. W., and Klein, S. A.: Evidence for climate change in the satellite cloud record, Nature, 536, 72–75, https://doi.org/10.1038/nature18273, 2016.

Reboita, M. S., Ambrizzi, T., Silva, B. A., Pinheiro, R. F., and da Rocha, R. P.: The South Atlantic Subtropical Anticyclone: Present and Future Climate, Frontiers in Earth Science, 7, https://doi.org/10.3389/feart.2019.00008, 2019.

Richter, I.: Climate model biases in the eastern tropical oceans: Causes, impacts and ways forward, Wiley Interdisciplinary Reviews: Climate Change, 6, 345–358, https://doi.org/https://doi.org/10.1002/wcc.338, 2015.

Richter, I. and Mechoso, C. R.: Orographic influences on the annual cycle of Namibian stratocumulus clouds, Geophysical Research Letters, 31, https://doi.org/https://doi.org/10.1029/2004GL020814, 2004.

Seethala, C., Norris, J. R., and Myers, T. A.: How Has Subtropical Stratocumulus and Associated Meteorology Changed since the 1980s?, Journal of Climate, 28, 8396 – 8410, https://doi.org/10.1175/JCLI-D-15-0120.1, 2015.

Staten, P. W., Lu, J., Grise, K. M., Davis, S. M., and Birner, T.: Re-examining Tropical Expansion, Nature Climate Change, 8, 768–775, https://doi.org/10.1038/s41558-018-0246-2, 2018.

Vicencio Veloso, J., Böhm, C., Schween, J. H., Löhnert, U., and Crewell, S.: A comparative study of the atmospheric water vapor in the Atacama and Namib Desert, Global and Planetary Change, 232, 104 320, https://doi.org/https://doi.org/10.1016/j.gloplacha.2023.104320, 2024.

Watanabe, M., Kang, S. M., Collins, M., Hwang, Y.-T., McGregor, S., and Stuecker, M. F.: Possible shift in controls of the tropical Pacific surface warming pattern, Nature, 630, 315–324, https://doi.org/https://doi.org/10.1038/s41586-024-07452-7, 2024.

Wood, R.: Stratocumulus Clouds, Monthly Weather Review, 140, 2373 – 2423, https://doi.org/https://doi.org/10.1175/MWR-D-11-00121.1, 2012.

Xu, H., Wang, Y., and Xie, S.-P.: Effects of the Andes on Eastern Pacific Climate: A Regional Atmospheric Model Study, Journal of Climate, 17, 589 – 602, https://doi.org/https://doi.org/10.1175/1520-0442(2004)017<0589:EOTAOE>2.0.CO;2, 2004.

Zelinka, M. D., Myers, T. A., McCoy, D. T., Po-Chedley, S., Caldwell, P. M., Ceppi, P., Klein, S. A., and Taylor, K. E.: Causes of Higher Climate Sensitivity in CMIP6 Models, Geophysical Research Letters, 47, e2019GL085 782, https://doi.org/https://doi.org/10.1029/2019GL085782, e2019GL085782 10.1029/2019GL085782, 2020.

Zhang, H., Zheng, Y., and Li, Z.: Improving low-cloud fraction prediction through machine learning, Geophysical Research Letters, 51, e2024GL109 735, https://doi.org/https://doi.org/10.1029/2024GL109735, 2024.